

Pressure-Induced Bandgap Optimization in Lead-Based Perovskites with Prolonged Carrier Lifetime and Ambient Retainability

HPSTAR
338-2017

Gang Liu,* Lingping Kong, Jue Gong, Wenge Yang, Ho-kwang Mao,* Qingyang Hu, Zhenxian Liu, Richard D. Schaller, Dongzhou Zhang, and Tao Xu*

Bond length and bond angle exhibited by valence electrons is essential to the core of chemistry. Using lead-based organic–inorganic perovskite compounds as an exploratory platform, it is demonstrated that the modulation of valence electrons by compression can lead to discovery of new properties of known compounds. Yet, despite its unprecedented progress, further efficiency boost of lead-based organic–inorganic perovskite solar cells is hampered by their wider bandgap than the optimum value according to the Shockley–Queisser limit. By modulating the valence electron wavefunction with modest hydraulic pressure up to 2.1 GPa, the optimized bandgap for single-junction solar cells in lead-based perovskites, for the first time, is achieved by narrowing the bandgap of formamidinium lead triiodide ($\text{HC}(\text{NH}_2)_2\text{PbI}_3$) from 1.489 to 1.337 eV. Strikingly, such bandgap narrowing is partially retained after the release of pressure to ambient, and the bandgap narrowing is also accompanied with double-prolonged carrier lifetime. With First-principles simulation, this work opens a new dimension in basic chemical understanding of structural photonics and electronics and paves an alternative pathway toward better photovoltaic materials-by-design.

solar light, the transporting property of the material, and the separation of the excited charges/holes. Among these factors, bandgap of the absorption layer is an intrinsic materials property that directly affects the applications in solar cell devices. According to Shockley–Queisser theory,^[8,9] the efficiency limit for single-junction semiconductor-based solar cells under AM1.5 solar spectrum and one-Sun illumination is 33.7%, which requires a corresponding optimum bandgap energy of 1.34 eV,^[8–11] much smaller than that of pristine $\text{CH}_3\text{NH}_3\text{PbI}_3$.^[12] Efforts to tune the bandgap by conventional chemical modifications lead to unwanted shorter carrier lifetime (substitution of Pb by Sn^[13,14]) and/or larger bandgaps (substitution of I by Cl and/or Br.^[15,16]) Therefore, a pressing need is to explore an alternative way with fundamental understanding to narrow the bandgap while retaining, if not improving, the desirable photovoltaic

1. Introduction

Almost never does a material exhibit such a land-sliding breakthrough as the organolead trihalide hybrid perovskites have achieved within the last six years in the photovoltaic community.^[1–7] For a multilayer thin film solar cell, the solar energy transform efficiency depends on many factors, including bandgap, the position of the valence band maximum/conduction band minimum (VBM/CBM), the overall absorption of the

merits of lead-based perovskites, particularly their long charge carrier lifetime that is crucial to their striking long carrier diffusion lengths.^[17–20] By applying controllable hydrostatic pressure on methylammonium lead trihalide ($\text{CH}_3\text{NH}_3\text{PbX}_3$, X = I[−] or Br[−]) perovskites, previous effort was able to narrow the material bandgaps through pressure-induced shrinkage in X–Pb–X bond lengths, but only for small extents before detrimental phase transition occurred,^[21–26] thereby making the approach of optimum bandgap still a basic science challenge.

Dr. G. Liu, Dr. L. Kong, Dr. W. Yang, Dr. H.-k. Mao
Center for High Pressure Science and Technology Advanced Research
Shanghai 201203, China
E-mail: liugang@hpstar.ac.cn; mao@gl.ciw.edu

Dr. G. Liu, Dr. L. Kong, Dr. W. Yang, Dr. H.-k. Mao, Dr. Q. Hu, Dr. Z. Liu
Geophysical Laboratory
Carnegie Institution of Washington
Washington, DC 20015, USA

J. Gong, Prof. T. Xu
Department of Chemistry and Biochemistry
Northern Illinois University
DeKalb, IL 60115, USA
E-mail: txu@niu.edu

Prof. R. D. Schaller
Center for Nanoscale Materials
Argonne National Laboratory
Argonne, IL 60439, USA

Dr. D. Zhang
Hawai'i Institute of Geophysics and Planetology
School of Ocean and Earth Science and Technology
University of Hawai'i at Manoa
Honolulu, HI 96822, USA



DOI: 10.1002/adfm.201604208

One key atomic-level understanding of the interplay between bandgap and lattice structures is the Pb–I–Pb bond angles. Our work indicates that the Pb–I–Pb in $\text{CH}_3\text{NH}_3\text{PbI}_3$ only aligned linearly along one dimension; thus, the compression causes inhomogeneous contraction of Pb–I–Pb in three dimensions, which eventually leads to detrimental bond angle variation, i.e., phase transition was triggered at above 0.3 GPa.^[24] Thus, seeking another Pb-based perovskite with linear Pb–I–Pb bonds along all three dimensions may bring about persistent bandgap narrowing under pressure while still keeping the attractive long carrier lifetime. Structurally analogous to $\text{CH}_3\text{NH}_3\text{PbI}_3$, $\text{HC}(\text{NH}_2)_2\text{PbI}_3$ (FAPbI₃) is composed of larger organic cation $\text{HC}(\text{NH}_2)_2^+$, with cationic charge distributed over its structure via the π system. As such, it may stretch and flatten out the kinked Pb–I–Pb bonds along the other two dimensions, as suffered by $\text{CH}_3\text{NH}_3\text{PbI}_3$. Plus, it has demonstrated comparable device efficiency and optoelectronic properties to those of $\text{CH}_3\text{NH}_3\text{PbI}_3$.^[27–30] Therefore, it is intriguing to study the properties of this material under elevated pressures.

Herein, we report a striking bandgap narrowing of FAPbI₃ from 1.489 to 1.337 eV when applied pressure is increased from 1 atm to 2.1 GPa. This is the first report on achieving the optimal bandgap required by Shockley–Queisser efficiency limit in lead-based hybrid perovskites. An exceptional

merit is that the narrowed bandgap is accompanied by carrier lifetime prolongation. The more thrilling fact is that the narrowed bandgap formed under high pressure condition is partially retainable after pressure is released back to 1 atm, revealing insightful interplay between the lattice structure and light-induced valence electronic properties in the chemical compounds. This work could substantially resolve the mechanistic foundation of hybrid lead halide perovskites and provide theoretical guidelines as well as engineering routes to significantly advance photovoltaic technology.

2. Results and Discussion

2.1. Bandgap Narrowing down to Shockley–Queisser Optimal Magnitude in Compressed FAPbI₃

We performed high-resolution synchrotron X-ray diffraction (XRD) to examine the crystal structure of the as-prepared FAPbI₃ samples. Results showed good fit between observed pattern and calculated result using trigonal $P3m1$ model, as evidenced by the tiny discrepancy factors ($R_p = 1.17\%$, $R_{wp} = 2.42\%$ see Figure 1a). Crystal lattice parameters were resolved to be $a = b = 9.000(1)$ Å, $c = 11.073(4)$ Å, $\alpha = 90^\circ$, $\gamma = 120^\circ$, in good

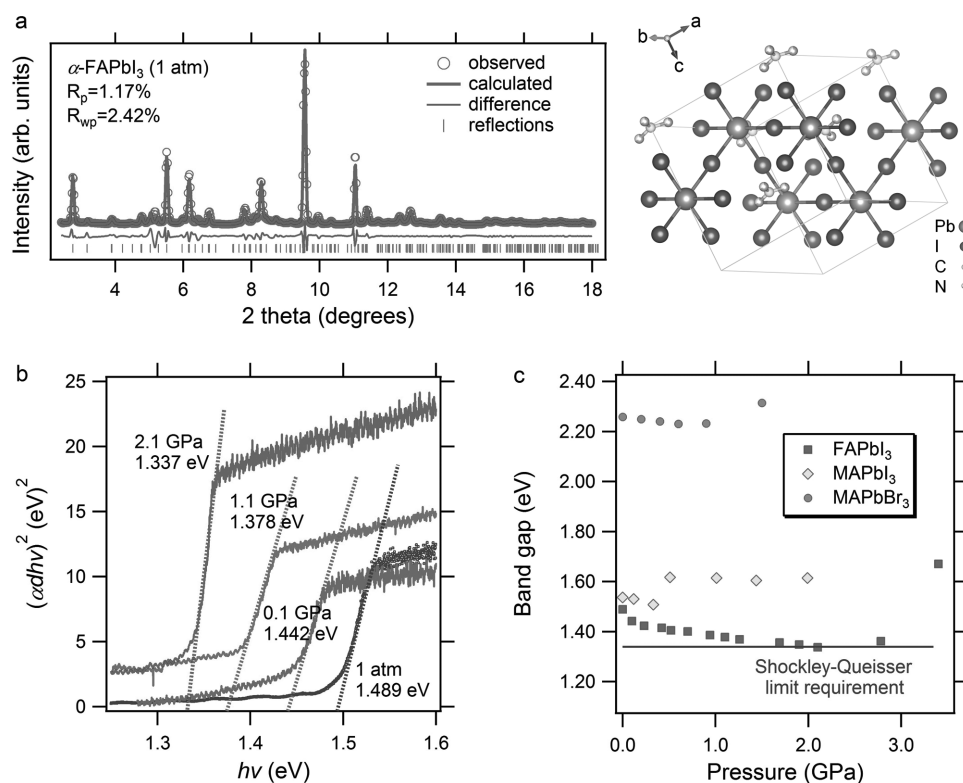


Figure 1. Direct experimental evidence of bandgap narrowing down to Shockley–Queisser optimal magnitude in compressed FAPbI₃. a) High-resolution synchrotron XRD pattern measured at ambient condition (1 atm) for as-prepared FAPbI₃ sample. The crystal structure can be well fitted using trigonal α -FAPbI₃ structure with $P3m1$ space group symmetry (blue open circle: experimental data; red line: calculated result; grey line: difference between calculation and experimental result; green bar: Bragg reflections of α -FAPbI₃). Schematic crystal structure of trigonal α -FAPbI₃ is also shown here. b) Direct bandgap Tauc plots of α -FAPbI₃ collected at 1 atm, 0.1 GPa, 1.1 GPa, and 2.1 GPa. Magnitudes of bandgaps can be estimated by extrapolating the linear portion of the Tauc plots to the baselines. Pressure-induced redshift of the bandgap gradually occurs from 1 atm up to 2.1 GPa, where the smallest magnitude 1.337 eV was observed, reaching the Shockley–Queisser optimal bandgap (1.34 eV). c) Pressure-dependent optical bandgap evolutions of FAPbI₃ (red), MAPbI₃^[24] (yellow), and MAPbBr₃^[24] (blue). The symbol size covers the size of the error bars.

agreement with reports on trigonal FAPbI_3 ($\alpha\text{-FAPbI}_3$).^[30–32] It was previously discovered that optical bandgaps of hybrid halide perovskite materials are pressure-dependent.^[21–24] In short, a redshift in bandgap with no less than 1.5 eV can be observed under mild pressure (<0.3 GPa), above which a phase transition occurs and the bandgap rebounds up.^[24] Surprisingly, however, the bandgap of $\alpha\text{-FAPbI}_3$ experienced a redshift from 1.489 to 1.337 eV as hydrostatic pressure was increased from 1 atm to 2.1 GPa, reaching the Shockley–Queisser optimum bandgap for the first time in lead-based hybrid perovskites (see Figure 1b, Supporting Information Note, and Figures S1–S3 in the Supporting Information). Shockingly, the magnitude of change in bandgap (0.15 eV) is significantly larger than MAPbI_3 (0.04 eV) and MAPbBr_3 (0.03 eV),^[22–24] as summarized in Figure 1c.

2.2. Structural Origin of Bandgap Evolution Under Pressure

To investigate the root course of the gigantic redshift found in $\alpha\text{-FAPbI}_3$, we conducted in situ synchrotron high pressure XRD experiments up to 7.0 GPa at room temperature (Figure 2). Figure 2a shows the typical XRD patterns of FAPbI_3 as a function of pressure. For the first test pressure at 0.4 GPa, crystal structure can be readily resolved using ambient phase with space group $P3m1$, as supported by the refinement with relatively small errors of R_p (1.05%) and R_{wp} (1.55%) (see Figure S4, Supporting Information). As pressure increases to 7.0 GPa, all XRD peaks of the continuously shifted to larger 2 theta (smaller d -spacing) range, while no new peak was observed. All patterns are consistent with the $P3m1$ structure and representative GSAS refinement results are listed in Tables S1–S3 (Supporting Information). Although the absence of crystal phase transition was demonstrated, for pressure higher than 2.5 GPa, anisotropic peak broadening was observed upon pressure increase and broad background originating from the diffuse scattering appeared, suggesting the occurrence of lattice distortion associated with significantly distorted PbI_6 octahedra.^[33–35] It is well known that the Pb–I–Pb bond angle represents the PbI_6 octahedral tilting, which is responsible for the changes in the electronic structure close to the band edges, thus determining the bandgap.^[36] For low-pressure phase $P3m1$, the Pb–I–Pb bond angle remains at nearly 180° along all three dimensions and the bond length shortens as the pressure increases (see Figure 2b and Tables S2 and S3, Supporting Information). The essence of electron–photon interaction in hybrid lead iodide mainly involves the transition of electrons from the I 5*p* states to the Pb 6*p* states and a small quantity of localized transition from Pb 6*s* to Pb 6*p*. Upon compression, the coupling between I 5*p* and Pb 6*p* orbitals pushes up the VBM. In contrast, the CBM is mostly a nonbonding localized state of Pb *p* orbitals, which is relatively insensitive to bond length or pressure. The net result, therefore, is the decrease in bandgap under pressures. We use first-principles calculations to investigate the electronic structure of FAPbI_3 from ambient pressure to 2.1 GPa (see Figure 2c and Figures S5–S11, Supporting Information). At 2.1 GPa, both experiment and simulation demonstrated the

narrowest bandgap, with 1.38 eV from simulation and 1.337 eV from optical absorbance experiment. However, as the pressure increases above 2.5 GPa, obvious lattice distortion and atomic displacement occurs, appearing as the XRD peaking broadening attributed to the distortion of the Pb–I–Pb bond. As such, the off-aligned Pb–I–Pb bond leads to less coupling between the Pb *s* and I *p* orbitals, and consequently results in the wider bandgap (see Figure S12, Supporting Information). This atomic distortion-driven (rather than amorphization-driven or phase transition-driven) bandgap blueshift in organic–inorganic hybrid perovskites has not been reported previously.

Notably, the absence of crystal phase transition in FAPbI_3 under pressure plays a pivotal role in an aggressive bandgap narrowing that reaches the optimal Shockley–Queisser bandgap for single-junction photovoltaic materials, as it allows a continuous bond length shrinkage (causing more overlapping between I 5*p* and Pb 6*p*) without bond angle distortion (causing less overlapping between I 5*p* and Pb 6*p*). Unlike methylammonium organic–inorganic perovskites, in which the Pb–I–Pb bond angle is aligned as nearly 180° only along one dimension, all the three Pb–I–Pb bond angles in $\alpha\text{-FAPbI}_3$ (trigonal $P3m1$ space group) exhibit $\approx 180^\circ$ (Figure 2b and Table S2, Supporting Information). The minimized PbI_6 octahedra tilting of $\alpha\text{-FAPbI}_3$ can also be evidenced by its smaller bandgap than MAPbI_3 through greater steric size of FA^+ according to studies.^[32,37,38] Spatially, the responses of the Pb–I–Pb bonds in FAPbI_3 to compression are similar and quasi-homogeneous. Then, a rational mechanistic understanding is that when all bond angles maintain $\approx 180^\circ$, as in the case of FAPbI_3 , the crystal undergoes a uniform compression that allows all atoms in the PbI_6 octahedra to remain their relative position to others, avoiding some preferential Pb–I–Pb bond bending (causing phase transition) as in the case of MAPbI_3 where $I4/mcm$ to $Imm2$ phase transition occurs at very mild pressure ≈ 0.4 GPa. Therefore, we believe it is the linear Pb–I–Pb geometry extending across the whole Pb–I framework that functions to withstand dislocation between Pb and I, thereby postponing the occurrence of structural phase transition. Additionally, compared to MA cations, a higher probability of forming hydrogen bonds between FA cations may also contribute to the structural stability of FAPbI_3 under pressure.

On the other hand, the highly compressible nature of the FAPbI_3 crystal is demonstrated by refinements on XRD patterns (Figure 2a), which yields the relative changes of lattice constants and volume, as shown in Figure 2d–f. Compared to methylammonium organic–inorganic perovskites including MAPbI_3 ,^[39] MASnI_3 ,^[40] and MAPbBr_3 ,^[41] lower bulk modulus K_0 was observed in FAPbI_3 , being on the order of 11.0(2) GPa (Figure 2g,h). Such a soft characteristic results in an effective electron orbitals overlapping even at very low pressures, thus significant bandgap narrowing can be expected. In comparison to the rigid C–N bond in MAPbI_3 , the bendable V-shaped N–C–N bond in FAPbI_3 allows flexible space needed for achieving high compressibility (Figures S14 and S15, Supporting Information). Indeed, a smaller bulk modulus ($K_0 = 8.0(7)$ GPa) was observed also in another formamidinium organic–inorganic hybrid iodide, namely, FASnI_3 .^[40]

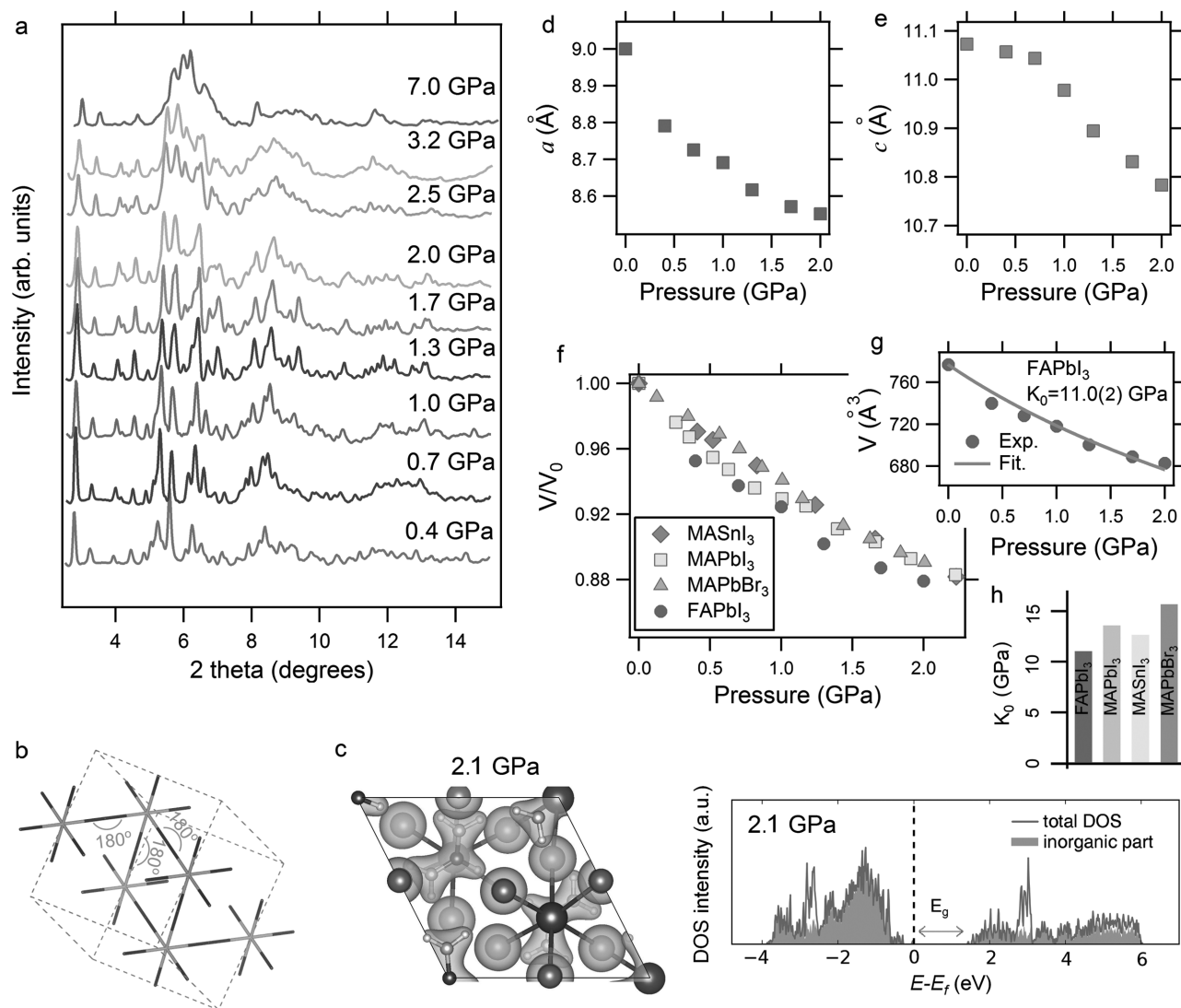


Figure 2. Pressure-induced structural evolution of FAPbI₃. a) Pressure-dependent in situ synchrotron angle dispersive X-ray diffraction patterns of FAPbI₃ in compression up to 7.0 GPa. The absence of crystal phase transition is concluded since no new peak can be identified. b) Pb–I inorganic framework of trigonal α -FAPbI₃, from which 3D $\approx 180^\circ$ Pb–I–Pb bond angles are highlighted. c) Charge density of FAPbI₃ at 2.1 GPa. Purple spheres: I atoms; grey atoms: Pb atoms. Panel (c) also shows the density of states (DOS) of FAPbI₃ at 2.1 GPa in which the magnitude of bandgap can be estimated. d,e) Pressure dependence of lattice constants *a* and *c* for α -FAPbI₃ unit cell. f) Pressure dependence of relative changes in lattice volume of MASnI₃ (blue), MAPbI₃ (yellow), MAPbBr₃ (green), and FAPbI₃ (red). Compared to methylammonium organic–inorganic perovskites,^[39–41] FAPbI₃ exhibits higher compressibility. g) The bulk modulus *K*₀ of FAPbI₃ was estimated to be 11.0(2) GPa by fitting experimental data with the Birch relation,

$$P(V) = \frac{3}{2}B_0 \left[\left(\frac{V_0}{V} \right)^{\frac{7}{3}} - \left(\frac{V_0}{V} \right)^{\frac{5}{3}} \right] \left\{ 1 + \frac{3}{4}(B' - 4) \left[\left(\frac{V_0}{V} \right)^{\frac{2}{3}} - 1 \right] \right\},$$

where we assume $B' = 4$. In panels (d)–(g), the symbol size covers the size of the error bars.

h) Comparison of *K*₀ values among FAPbI₃ (red), MAPbI₃ (orange), MASnI₃ (yellow), and MAPbBr₃ (blue). In panels (f) and (h), the data for MASnI₃ and MAPbI₃ are from refs. [40] and [41], respectively. For MAPbI₃, we estimated the *K*₀ to be 13.6(5) GPa by fitting experimental data in ref. [39] (see Figure S13 in the Supporting Information for details).

2.3. Significant Prolongation of Carrier Lifetime

We further conducted static and dynamic in situ high pressure photoluminescence (PL) measurements on FAPbI₃ to examine the pressure dependence of carrier lifetime (Figure 3), a decisive quantity for attaining the near-bandgap photovoltage and for the solar cell device performance.^[6,19,20] The defect-related trap states in MAPbI₃ are believed to be located in shallower levels close to band edges, thus the electron–hole pair recombination

is easily prohibited.^[42,43] Compared to MAPbI₃, FAPbI₃ exhibits shorter carrier lifetime,^[44] suggesting higher trap density and/or deeper trap levels.^[45] As the bandgap narrows under compression (Figure 1), the previously deep states become relatively closer to band edges, i.e., shallower traps, leading to longer carrier lifetime. Figure 3a and its inset show the pressure-driven evolutions of the static PL spectrum and the main PL peak position, respectively. The pronounced redshift of PL peak position from 810 nm at ambient condition to 872 nm at

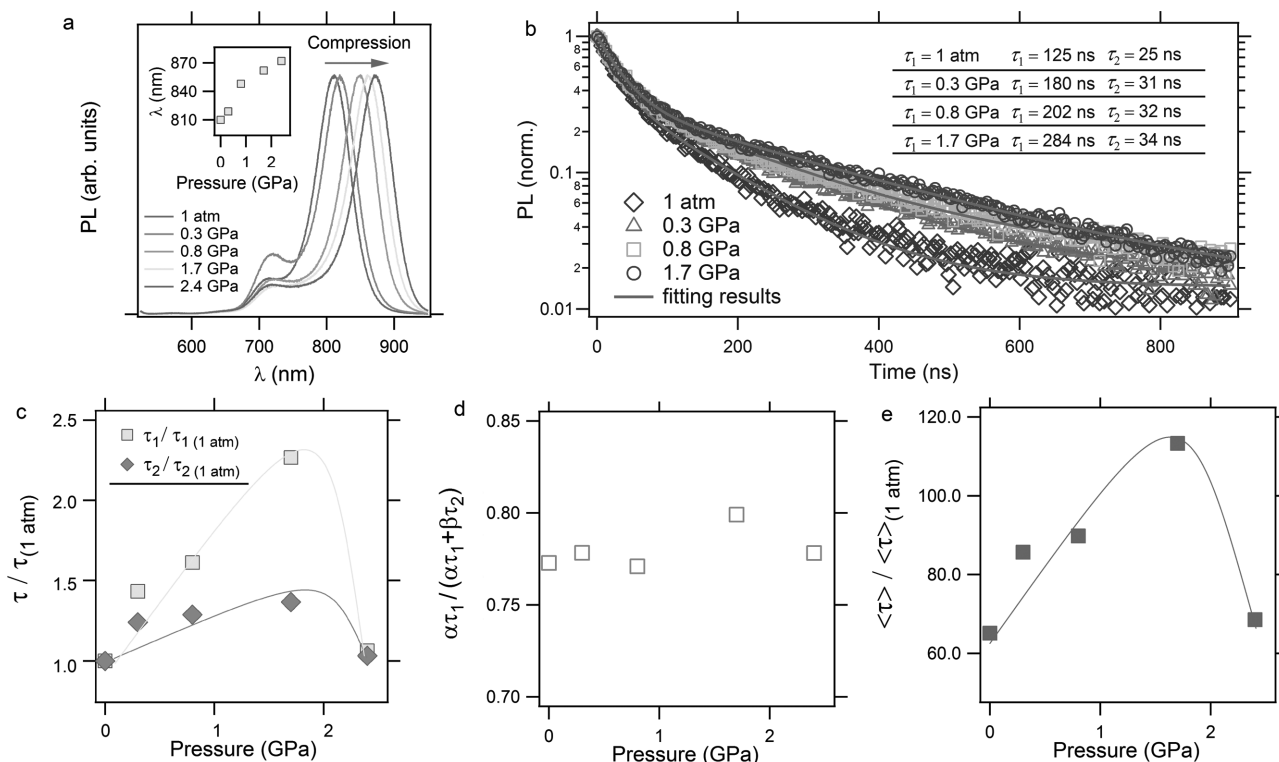


Figure 3. Carrier lifetime prolongation of α -FAPbI₃ upon compression. a) Pressure-dependent static PL signal in compression. The inset shows the redshift of main peak position. b): in situ high pressure dynamic PL measurements on an FAPbI₃ sample at 1 atm, 0.3 GPa, 0.8 GPa, and 1.7 GPa. For all measured pressures, both slow (τ_1) and fast (τ_2) components of carrier lifetime were determined using biexponential fittings ($I_{\text{PL}}(t) = I_{\text{int}}[\alpha \cdot \exp(-t/\tau_1) + \beta \cdot \exp(-t/\tau_2) + I_0]$) on time decay traces. c) Pressure dependence relative changes in τ_1 and τ_2 . d) Pressure dependence of the relative contribution of the bulk-dominated slow component, $\alpha\tau_1/(\alpha\tau_1 + \beta\tau_2)$. e) Pressure dependence of the normalized mean carrier lifetime, $\langle \tau \rangle / \langle \tau \rangle(1 \text{ atm})$, where $\langle \tau \rangle = [\alpha\tau_1/(\alpha\tau_1 + \beta\tau_2)]\tau_1 + [\beta\tau_2/(\alpha\tau_1 + \beta\tau_2)]\tau_2$. Peak values in carrier lifetimes of FAPbI₃ were observed at 1.7 GPa, where a dramatic increase in τ_1 by 120% has been demonstrated. In panels (c)–(e), the symbol size covers the size of the error bars. In panels (c) and (e), the lines are the guide for the eye and not the fit to the data.

2.4 GPa is in agreement with the observed trend of bandgap narrowing upon compression. For dynamic (time-resolved) PL measurements, the data were measured at the wavelength of respective main static PL peaks. Our high pressure PL and time-resolved PL measurement was carried out on the same piece of polycrystalline sample in compression to exclude the various defect states among different samples. PL time decay traces at various pressures were collected in Figure 3b, and all time-resolved traces were fitted by an biexponential decay function $I_{\text{PL}}(t) = I_{\text{int}}[\alpha \cdot \exp(-t/\tau_1) + \beta \cdot \exp(-t/\tau_2) + I_0]$ to quantify the PL decay dynamics, where the slow component τ_1 and the fast component τ_2 are assigned to free carrier recombination in the bulk and on the surface, respectively.^[19]

At ambient pressure, the FAPbI₃ sample has a superposition of slow and fast dynamics, being the order of 125 and 25 ns (Figure 3b), respectively. Interestingly, both slow and fast components exhibit an obvious rise in compression. At 1.7 GPa, the carrier lifetime reaches a peak value of 284 ns, over two times longer than that at ambient pressure (Figure 3b,c). As the applied pressure further increased to 2.4 GPa, a dramatic decrease in carrier lifetime was observed (see Table S4, Supporting Information), which can be attributed to the fact that more defective states were generated at higher pressures due to the emergence of atomic distortion.

At every tested pressure, the relative contribution of the slow component to the static PL amounts to a stable value of over 77% (Figure 3d), thus the pressure-driven carrier lifetime prolongation is a bulk-related intrinsic phenomenon. Taking the account of the relative contribution of the slow and fast components, we evaluated the mean carrier lifetime $\langle \tau \rangle$ defined as $[\alpha\tau_1/(\alpha\tau_1 + \beta\tau_2)]\tau_1 + [\beta\tau_2/(\alpha\tau_1 + \beta\tau_2)]\tau_2$, and an increase in $\langle \tau \rangle$ of over 70% was achieved at 1.7 GPa (see Figure 3e and Table S4, Supporting Information).

2.4. Retainable Structural and Electronic Properties

To seek the potential usefulness of the pressure-induced bandgap narrowing for practical applications, we investigated the retainability of the narrowed bandgap after pressure is completely released (Figure 4). By subtracting the measured transmission spectra (see Figure 4a) of the silicon oil background from that of the decompressed FAPbI₃ sample (in silicon oil) from 7.1 GPa to 1 atm, the absorbance and transmittance spectra of the sample were obtained, as shown in Figure 4b. Clearly, sharp absorbance and transmittance onsets are presented around 870 nm. By extrapolating the linear portion of the $(\alpha\text{d}h\nu)^2$ versus photonic energy $h\nu$, a direct bandgap of 1.447 eV

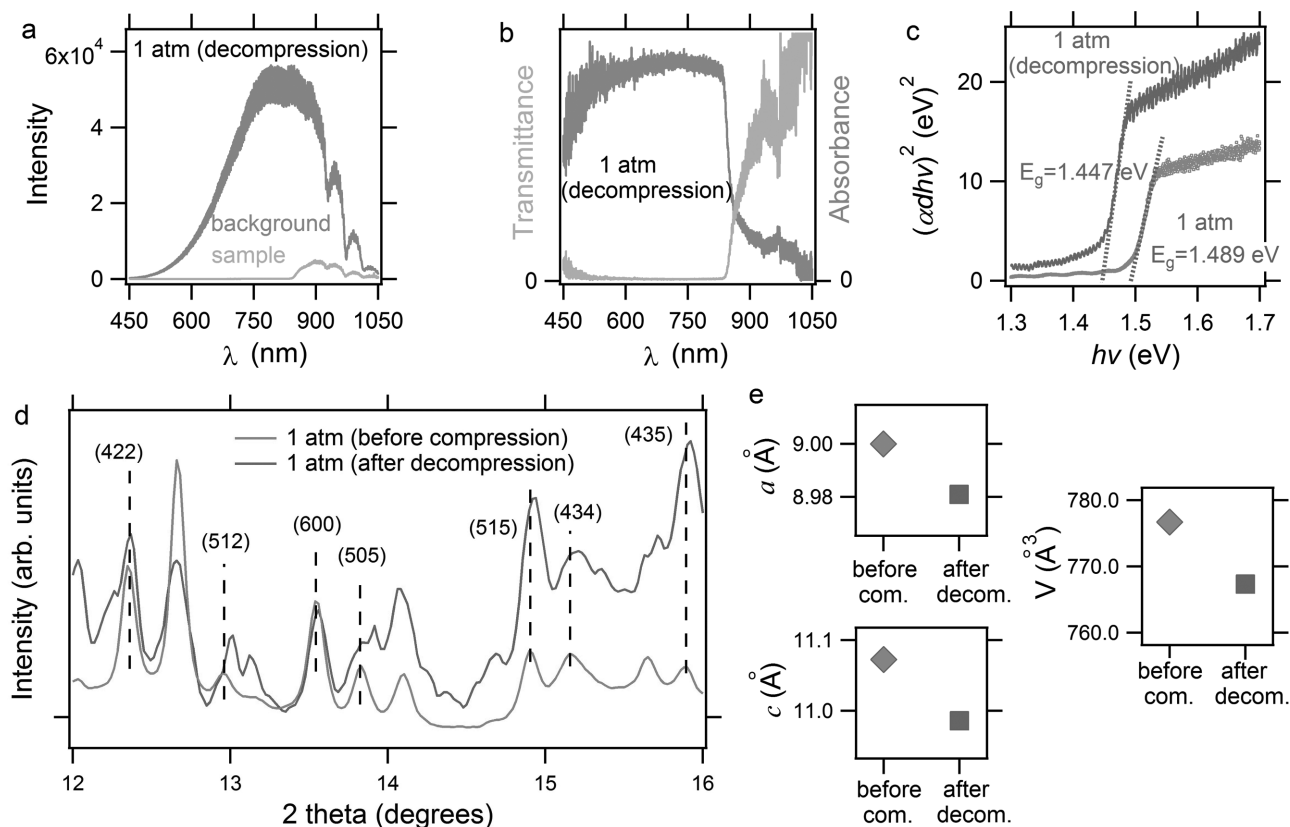


Figure 4. Partial retainable bandgap observed in FAPbI₃. a) Collected transmission spectra of the silicon oil background and FAPbI₃ sample (in the oil) after decompression back to 1 atm from 7.1 GPa. b) The absorbance and transmittance spectra of the decompressed sample were then obtained, and sharp absorbance (blue) and transmittance (orange) onsets are observed around 870 nm. c) Tauc plots for FAPbI₃ before compression (grey) and after decompression (red). Bandgap magnitudes were determined to be 1.489 eV before compression and 1.447 eV after decompression for FAPbI₃. Such a ≈42 meV decrease convinces the photonic retainability after applied pressure is totally released. d) Comparison of powder X-ray diffraction pattern before compression (blue) and after decompression (red). Clearly, after decompression diffraction peaks shift toward higher 2 theta (lower *d*-spacing) range, demonstrating that the quenched unit cell remembers some high pressure information. e) Comparisons of lattice parameters *a* (left upper), *c* (left lower), and cell volume (right) before compression and after decompression. The symbol size covers the size of the error bars.

was estimated for the decompressed sample, which is 42 meV lower than that before compression (1.489 eV, see Figure 1b). To explore the structural origin of such enhanced optical property, we compared the XRD patterns before compression and after decompression for the same FAPbI₃ sample. Echoing the bandgap, the crystal structure also exhibits a partial retainable behavior, as evidenced by the fact that all XRD peaks shifted to larger 2 theta range after the pressure is released (Figure 4d). Correspondingly, for the decompressed sample, the lattice constants and volume were estimated to be *a* = 8.981(2) Å, *c* = 10.986(3) Å, and *V* = 767.340(3) Å³, obviously smaller than those in the sample before compression (*a* = 9.000(1) Å, *c* = 11.073(4) Å, and *V* = 776.706(4) Å³) (Figure 4e), meaning the structural information at high pressure is memorized by the sample after pressure is released. Therefore, the retainability of bandgap narrowing from high pressure condition can be readily understood by the observed structural plasticity of FAPbI₃, namely, the nonreversible lattice shrinkage in response to the applied pressure. Due to the facility characteristics of diamond anvil cell (DAC) employed in this work, the size of pressurized sample is 20–30 μm. Although such a small-sized sample could not be enough for a real solar cell device

fabrication, our results pave a promising pace to have high performance materials, and large-volume press high pressure facility^[46,47] could help us to obtain a large volume of pressurized FAPbI₃ sample with narrower bandgap.

3. Conclusion

Our study unprecedentedly achieved the optimal Shockley–Queisser bandgap in organic–inorganic lead trihalide perovskites using a clean physical tool, i.e., compression, and revealed key fundamental mechanics that govern the structure–materials property relationship in hybrid perovskite materials. More strikingly, two benign phenomena are accompanied with the narrowed bandgap, including the elongated carrier lifetime and the retainability of the narrowed bandgap after pressure is released. Our discovery suggests that pressure is an effective tool to tune the key materials properties by modulating their lattice structure in a precise and controllable manner, thus to achieve better materials-by-design toward tunable, improved, and retainable performance for next-generation photovoltaic and semiconductor systems.^[48–50]

4. Experimental Section

Chemicals and Reagents: Hydroiodic acid (HI, 57% w/w aqueous solution), lead(II) iodide (PbI_2 , 99.9985% metals basis), and *N,N*-Dimethylformamide (DMF, anhydrous, 99.8%) were purchased from Alfa Aesar. Formamidinium acetate (FAAc, 99%) and γ -Butyrolactone ($\geq 99\%$) were purchased from Aldrich. Lead acetate ($\text{Pb}(\text{ac})_2 \cdot 3\text{H}_2\text{O}$) was purchased from Mallinckrodt. Diethyl ether and acetonitrile (HPLC grade) were purchased from Fisher Chemical. All chemicals were used directly as received without further purification.

Synthesis of FAI and FAPbI_3 : FAI was synthesized by drop-wise introducing 16.0 mL HI to 12.1130 g FAAc in a 100 mL round-bottom flask immersed in ice bath, with stirring in solution. FAAc and HI were allowed to react for 12 h. The resulting solution was subsequently rotary evaporated at 60 °C until dry white–yellow solid formed. Collected solid was washed with diethyl ether and followed by vacuum filtration for six times. Pure compound was obtained by further drying in an oven at 110 °C for 12 h. 1:1 molar ratio of FAI and PbI_2 were dissolved in DMF to make a 0.88 M perovskite solution. Precursor solution was heated at 80 °C with stirring for 1 h, and then was hot-casted onto a pre-cleaned ZnSe substrate (Thorlabs). After the solvent evaporated, black FAPbI_3 polycrystals were collected by carefully scraping down the glass slide using a plastic slide.

In Situ Synchrotron High Pressure Powder XRD: In situ synchrotron high pressure powder XRD experiments were carried out at 16-BM-D of the Advanced Photon Source (APS), Argonne National Laboratory (ANL). Monochromatic X-ray with wavelength of 0.3066 Å was employed and the incident X-ray beam was focused to $4 \times 5 \mu\text{m}^2$ spot. XRD patterns were collected with a MAR345 CCD detector. The samples were loaded in a symmetric type DAC with a pair of 300 μm culets and placed in a rhenium (Re) gasket hole with a diameter of 140 μm drilled by a laser micromatching system.^[51] Silicon oil was used as pressure-transmitting medium. It should be noted that methanol/ethanol cannot be used as the organic–inorganic hybrid samples are easily decomposed in water and/or polar solvent. Two ruby balls with diameters being on the order of 10 μm were loaded in the sample chamber. The pressure was determined by the ruby luminescence method. Such a pressure method was also employed in other high pressure experiments in this work, including high pressure optical absorbance measurement, and high pressure static PL and time-resolved PL dynamics experiment. GSAS program was employed to refine the obtained experimental XRD profiles.^[52] Figure S17 (Supporting Information) shows the optical images of FAPbI_3 in a DAC at various pressures.

In Situ High Pressure Optical Absorption Spectroscopy: In situ high pressure optical absorption spectroscopy was conducted at the Infrared Lab of the National Synchrotron Light Source II (NSLS II) at Brookhaven National Laboratory (BNL). The visible absorption measurements between 10 000 and 25 000 cm^{-1} utilized a customized visible microscope system.^[53] A symmetric type DAC and a pair of Ila-type diamond anvils with the culets size of 300 μm were employed. Silicon oil was used as pressure transmitting medium and the silicon oil spectra were used to determine an absorbance baseline.

In Situ High Pressure PL: In situ high pressure PL measurement was conducted at the Center for Nanoscale Materials, ANL. To measure static PL, FAPbI_3 samples were photoexcited at 450 nm and 40 nJ cm^{-2} via a 35 ps pulse-width laser diode. PL photons were collected with a lens and directed to a 300 mm focal-length grating spectrograph outfitted with a thermoelectrically cooled CCD and avalanche photodiode with time-correlated single-photon-counting electronics. The sample was loaded in Mao-type symmetric DAC with a pair of 300 μm culets and placed in an Re gasket hole with diameter being on the order of 140 μm . Silicon oil was used as pressure transmitting medium which provides good chemical inertness and hydrostatic condition.

First-Principles Computer Simulations: The calculations were performed in the framework of density functional theory through Vienna ab initio simulation package.^[54] The generalized gradient approximation under Perdew–Burke–Ernzerhof parametrization^[55] was implemented to describe the exchange correlation functions. The projected-augmented

wave potentials were used with 14 valence electrons for Pb ($5d^{10}6s^26p^2$), seven for I ($5s^25p^2$), four for C atoms ($2s^22p^2$), five for N atoms ($2s^22p^3$), and one for H ($1s^1$). A plane-wave basis set was used with kinetic 500 eV energy cutoff that is sufficient to optimize the structure until forces acting on each atom are less than 0.02 eV Å⁻¹. Monkhorst mesh of $5 \times 5 \times 5$ *k* points was employed for the *P3m1* FAPbI_3 . Pressure was applied by adding pulay stress to the diagonal elements of the stress tensor. The crystal band structures were sampled along the high-symmetry points (Γ -A-L-M- Γ -K-H- Γ) in the Brillouin zone.

Supporting Information

Supporting Information is available from the Wiley Online Library or from the author.

Acknowledgements

This project was supported by NSAF (Grant No. U1530402) and National Science Foundation (Grant No. CBET-1150617). High pressure powder structure characterizations were performed at beamline 16-BM-D at HPCAT, APS, ANL. HPCAT operations were supported by DOE-NSA under Award No. DE-NA0001974 and DOE-BES under Award No. DE-FG02-99ER45775, with partial instrumentation funding by the National Science Foundation (NSF). Part of this work was also performed at the Center for Nanoscale Materials (CNM), ANL, and the Infrared Lab of the National Synchrotron Light Source (NSLS II), Brookhaven National Laboratory (BNL). The use of APS and CNM facilities was supported by the U.S. Department of Energy, Office of Science, Office of Basic Energy Sciences (DE-AC02-06CH11357). The Infrared Lab was supported by National Science Foundation (EAR 1606856, COMPRES) and DOE/NSA (DE-NA-0002006, CDAC). The authors also thank Dr. Victor V. Ryzhov for his experimental support and Dr. H. Sheng for useful discussions. The computational work was conducted on the SR10000-K1/52 supercomputing facilities of the Institute for Materials Research, Tohoku University.

Received: August 15, 2016

Revised: October 12, 2016

Published online: December 5, 2016

- [1] A. Kojima, K. Teshima, Y. Shirai, T. Miyasaka, *J. Am. Chem. Soc.* **2009**, *131*, 6050.
- [2] J.-H. Im, I.-H. Jang, N. Pellet, M. Grätzel, N.-G. Park, *Nat. Nanotechnol.* **2014**, *9*, 927.
- [3] M. Kaltenbrunner, G. Adam, E. D. Glowacki, M. Drack, R. Schwödianer, L. Leonat, D. H. Apaydin, H. Groiss, M. C. Scharber, M. S. White, N. S. Sariciftci, S. Bauer, *Nat. Mater.* **2015**, *14*, 1032.
- [4] M. A. Green, A. Ho-Baillie, H. J. Snaith, *Nat. Photonics* **2014**, *8*, 506.
- [5] N. J. Jeon, J. H. Noh, Y. C. Kim, W. S. Yang, S. Ryu, S. I. Seok, *Nat. Mater.* **2014**, *13*, 897.
- [6] W. Nie, H. Tsai, R. Asadpour, J.-C. Blancon, A. J. Neukirch, G. Gupta, J. J. Crochet, M. Chhowalla, S. Tretiak, M. A. Alam, H.-L. Wang, A. D. Mohite, *Science* **2015**, *347*, 522.
- [7] W. Chen, Y. Wu, Y. Yue, J. Liu, W. Zhang, X. Yang, H. Chen, E. Bi, I. Ashraf, M. Grätzel, L. Han, *Science* **2015**, *350*, 944.
- [8] A. J. Nozik, *Nat. Photonics* **2012**, *6*, 272.
- [9] W. Shockley, H. J. Queisser, *J. Appl. Phys.* **1961**, *32*, 510.
- [10] W. E. I. Sha, X. Ren, L. Chen, W. C. H. Choy, *Appl. Phys. Lett.* **2015**, *106*, 221104.
- [11] M. I. Saidaminov, A. L. Abdelhady, G. Maculan, O. M. Bakr, *Chem. Commun.* **2015**, *51*, 17658.

- [12] F. Li, C. Ma, H. Wang, W. Hu, W. Yu, A. D. Sheikh, T. Wu, *Nat. Commun.* **2015**, *6*, 82338.
- [13] F. Hao, C. C. Stoumpos, D. H. Cao, R. P. H. Chang, M. G. Kanatzidis, *Nat. Photonics* **2014**, *8*, 489.
- [14] E. S. Parrott, R. L. Milot, T. Stergiopoulos, H. J. Snaith, M. B. Johnston, L. M. Herz, *J. Phys. Chem. Lett.* **2016**, *7*, 1321.
- [15] T. M. Brenner, D. A. Egger, L. Kronik, G. Hodes, D. Cahen, *Nat. Rev. Mater.* **2016**, *1*, 15007.
- [16] B. Luo, Y.-C. Pu, S. A. Lindley, Y. Yang, L. Lu, Y. Li, X. Li, J. Z. Zhang, *Angew. Chem., Int. Ed.* **2016**, *55*, 8864.
- [17] S. D. Stranks, G. E. Eperon, G. Grancini, C. Menelaou, M. J. P. Alcocer, T. Leijtens, L. M. Herz, A. Petrozza, H. J. Snaith, *Science* **2013**, *342*, 341.
- [18] G. Xing, N. Mathews, S. Sun, S. S. Lim, Y. M. Lam, M. Grätzel, S. Mhaisalkar, T. C. Sum, *Science* **2013**, *342*, 344.
- [19] D. Shi, V. Adinolfi, R. Comin, M. Yuan, E. Alarousu, A. Buin, Y. Chen, S. Hoogland, A. Rothenberger, K. Katsiev, Y. Losovyj, X. Zhang, P. A. Dowben, O. F. Mohammed, E. H. Sargent, O. M. Bakr, *Science* **2015**, *347*, 519.
- [20] C. Wehrenfennig, G. E. Eperon, M. B. Johnston, H. J. Snaith, L. M. Herz, *Adv. Mater.* **2014**, *26*, 1584.
- [21] Y. Wang, X. Lü, W. Yang, T. Wen, L. Yang, X. Ren, L. Wang, Z. Lin, Y. Zhao, *J. Am. Chem. Soc.* **2015**, *137*, 11144.
- [22] S. Jiang, Y. Fang, R. Li, H. Xiao, J. Crowley, C. Wang, T. J. White, W. A. Goddard, Z. Wang, T. Baikie, J. Fang, *Angew. Chem., Int. Ed.* **2016**, *55*, 6540.
- [23] A. Jaffe, Y. Lin, C. M. Beavers, J. Voss, W. L. Mao, H. I. Karunadasa, *ACS Cent. Sci.* **2016**, *2*, 201.
- [24] L. Kong, G. Liu, J. Gong, Q. Hu, R. D. Schaller, P. Dera, D. Zhang, Z. Liu, W. Yang, K. Zhu, Y. Tang, C. Wang, S.-H. Wei, T. Xu, H.-k. Mao, *Proc. Natl Acad. Sci. USA* **2016**, *113*, 8910.
- [25] L. Wang, K. Wang, B. Zou, *J. Phys. Chem. Lett.* **2016**, *7*, 2556.
- [26] D. Umeyama, Y. Lin, H. I. Karunadasa, *Chem. Mater.* **2016**, *28*, 3241.
- [27] J.-W. Lee, D.-J. Seol, A.-N. Cho, N.-G. Park, *Adv. Mater.* **2014**, *26*, 4991.
- [28] A. A. Zhumekenov, M. I. Saidaminov, M. A. Haque, E. Alarousu, S. P. Sarmah, B. Murali, I. Dursun, X.-H. Miao, A. L. Abdelhady, T. Wu, O. F. Mohammed, O. M. Bakr, *ACS Energy Lett.* **2016**, *1*, 32.
- [29] G. E. Eperon, S. D. Stranks, C. Menelaou, M. B. Johnston, L. M. Herz, H. J. Snaith, *Energy Environ. Sci.* **2014**, *7*, 982.
- [30] S. Pang, H. Hu, J. Zhang, S. Lv, Y. Yu, F. Wei, T. Qin, H. Xu, Z. Liu, G. Cui, *Chem. Mater.* **2014**, *26*, 1485.
- [31] C. C. Stoumpos, C. D. Malliakas, M. G. Kanatzidis, *Inorg. Chem.* **2013**, *52*, 9019.
- [32] A. Amat, E. Mosconi, E. Ronca, C. Quarti, P. Umari, M. K. Nazeeruddin, M. Grätzel, F. D. Angelis, *Nano Lett.* **2014**, *14*, 3608.
- [33] H. P. Klug, L. E. Alexander, *X-Ray Diffraction Procedures*, Wiley, New York **1954**.
- [34] T. Ungár, *Scr. Mater.* **2004**, *51*, 777.
- [35] R. Delhez, T. H. de Keijser, E. J. Z. Mittemeijer, *Anal. Chem.* **1982**, *54*, 312, 1.
- [36] C. C. Stoumpos, M. G. Kanatzidis, *Acc. Chem. Res.* **2015**, *48*, 2791.
- [37] M. R. Filip, G. E. Eperon, H. J. Snaith, F. Giustino, *Nat. Commun.* **2014**, *5*, 5757.
- [38] J. H. Lee, J.-H. Lee, E.-H. Kong, H. M. Jang, *Sci. Rep.* **2016**, *6*, 21687.
- [39] F. Capitani, C. Marini, S. Caramazza, P. Postorino, G. Garbarino, M. Hanfland, A. Pisanu, P. Quadrelli, L. Malavasi, *J. Appl. Phys.* **2016**, *119*, 185901.
- [40] Y. Lee, D. B. Mitzi, P. W. Barnes, T. Vogt, *Phys. Rev. B* **2003**, *68*, 020103.
- [41] I. P. Swainson, M. G. Tucker, D. J. Wilson, B. Winkler, V. Milman, *Chem. Mater.* **2007**, *19*, 2401.
- [42] M. B. Johnston, L. M. Herz, *Acc. Chem. Res.* **2016**, *49*, 146.
- [43] W.-J. Yin, T. Shi, Y. Yan, *Appl. Phys. Lett.* **2014**, *104*, 063903.
- [44] Q. Han, S.-H. Bae, P. Sun, Y.-T. Hsieh, Y. Yang, Y. S. Rim, H. Zhao, Q. Chen, W. Shi, G. Li, Y. Yang, *Adv. Mater.* **2016**, *28*, 2253.
- [45] W.-J. Yin, J.-H. Yang, J. Kang, Y. Yan, S.-H. Wei, *J. Mater. Chem. A* **2015**, *3*, 8926.
- [46] Y. Wang, M. Rivers, S. Sutton, N. Nishiyama, T. Uchida, T. Sanehira, *Phys. Earth Planet. Inter.* **2009**, *174*, 270.
- [47] J. Guignard, W. A. Crichton, *Rev. Sci. Instrum.* **2015**, *86*, 085112.
- [48] L. Dou, A. B. Wong, Y. Yu, M. Lai, N. Kornienko, S. W. Eaton, A. Fu, C. G. Bischak, J. Ma, T. Ding, N. S. Ginsberg, L.-W. Wang, A. P. Alivisatos, P. Yang, *Science* **2015**, *349*, 1518.
- [49] D. Zhang, S. W. Eaton, Y. Yu, L. Dou, P. Yang, *J. Am. Chem. Soc.* **2015**, *137*, 9230.
- [50] A. B. Wong, M. Lai, S. W. Eaton, Y. Yu, E. Lin, L. Dou, A. Fu, P. Yang, *Nano Lett.* **2015**, *15*, 5519.
- [51] R. Hrubciak, S. Sinogeikin, E. Rod, G. Shen, *Rev. Sci. Instrum.* **2015**, *86*, 072202.
- [52] A. C. Larson, R. B. von Dreele, *General structure analysis system (GSAS)*, Los Alamos National Laboratory Report LAUR **1994**, 86-748.
- [53] A. Jaffe, Y. Lin, W. L. Mao, H. I. Karunadasa, *J. Am. Chem. Soc.* **2015**, *137*, 1673.
- [54] G. Kresse, J. Hafner, *Phys. Rev. B* **1994**, *49*, 14251.
- [55] J. P. Perdew, K. Burke, M. Ernzerhof, *Phys. Rev. Lett.* **1996**, *77*, 3865.